DOI: https://doi.org/10.68732/f822bca9aaaa0bff

ISBN: 978-9989-2053-6-1

Computer-Aided Selection of Pillar Geometry in Deep Room-and-Pillar Panels Using Calibrated Large-Scale 3D FEM

K. Fuławka, P. Mertuszka & L. Stolecki
KGHM CUPRUM Ltd. Research & Development Centre, Wrocław, Poland
krzysztof.fulawka@kghmcuprum.com
0000-0002-0534-0712

M. Malesza, R. Wasilewski
KGHM Polska Miedź S.A, „Rudna Mine", Polkowiece, Poland

Abstract

Room-and-pillar mining at great depth must balance two competing targets: keeping the roof–pillar system stable under high in-situ stresses while maintaining high extraction. In panels affected by stress redistribution from nearby mined-out areas, empirical rules and simplified models may miss full-scale interactions and local damage, which can lead to sub-optimal design choices.

To support variant selection, a full-scale 3D finite element model was developed for a high-risk panel in the Rudna copper mine (Poland). The model domain (1.5 × 1.5 × 1.0 km) was implemented in GTS NX and used the Generalized Hoek–Brown failure criterion with GSI-based rock mass reduction. Mining-induced degradation was represented by assigning different parameter sets to key geomechanical zones (intact rock mass, large protective pillars, technological pillars, and mined-out/backfilled areas). The model was iteratively calibrated against in-situ convergence measurements from multiple monitoring locations to obtain a realistic deformation response.

Three room-and-pillar layouts were analysed with staged excavation reflecting mining advance and the liquidation phase with 4×3 m remnant pillars. The tested pillar geometries were 4×4 m, 5×6 m, and 8×8 m. The simulations showed clear differences in stability factor distribution and roof deflection behaviour. The 4×4 m variant produced unstable zones (FS < 1). The 8×8 m variant achieved the highest recovery (~93%), but it also indicated a stiff response and rapid loss of load-bearing capacity during pillar cutting, which may increase the likelihood of dynamic roof behaviour and elevated seismic risk. The 5×6 m variant offered the most balanced outcome, with acceptable stability (FS ≈ 1.1), high recovery (~90%), and a more controlled roof deflection process.

These results show that a calibrated full-scale 3D FEM model can be used as a practical decision tool to compare deep room-and-pillar variants, quantify safety margins, and select layouts that maximise recovery without compromising stability.

Keywords

Deep mining, Room-and-pillar mining, 3D numerical modelling, Finite element method, Hoek–Brown criterion.

1 Introduction

Room-and-pillar mining at great depth must balance roof–pillar stability under high in-situ stress with high extraction and operational efficiency. The challenge extends beyond tributary-area loading to progressive damage, confinement changes, and potential dynamic response linked to mining-induced seismicity (Fuławka et al., 2018). Key design choices—pillar geometry, opening size, sequencing and liquidation—interact in 3D and are influenced by neighbouring mined-out areas and stiffness contrasts (Jing, 2003; Shapka-Fels and Elmo, 2022). Although pillar design has long relied on empirical rules, their reliability decreases when extrapolated to greater depths, different lithologies or modified extraction sequences, where brittle spalling and progressive failure can drive non-linear behaviour (Hedley and Grant, 1972; Rafiei Renani and Martin, 2018). Numerical modelling is therefore increasingly used to capture 3D stress redistribution, excavation sequence effects and yielded zone development (Jing, 2003; Sinha and Walton, 2019). Predicted stability, however, depends on constitutive assumptions and the representation of damage and post-peak behaviour—especially when layouts have similar recovery but different deformation character and hazard potential (Sinha and Walton, 2019; Esterhuizen et al., 2011; Rafiei Renani and Martin, 2018). Reliability is typically improved using rock-mass strength frameworks such as Hoek–Brown and GSI, which support consistent parameter reduction and practical numerical implementation (Hoek et al., 1998; Hoek et al., 2002; Marinos et al., 2005; Benz et al., 2008).

Recent studies from the Lower Silesian Copper Basin confirm the value of staged modelling linked to observations, including frequency-dependent dynamic response analyses and large-scale 3D identification of increased seismic-risk zones validated with monitoring (Fuławka et al., 2022; Fuławka et al., 2024), as well as practical rockburst risk screening based on modelling outputs (Pytel et al., 2023). Against this background, this study presents a computer-aided workflow using a calibrated full-scale 3D FEM model (based on convergence monitoring) to compare feasible room-and-pillar variants for a deep, high-risk panel and support transparent selection by linking stability and deformation indicators with recovery-based economic screening (Esterhuizen et al., 2011; Sinha and Walton, 2019; Theron and Malan, 2024).

2 Geological and Mining Setting

The analysed panel lies at ~1,230 m depth and exploits a thin, stratiform orebody (~1.5 m on average; locally 0.6–2.4 m). The deposit dips gently (2–6°) and the ~380 m mining front makes stress redistribution and roof response sensitive to local geometry and neighbouring mined-out areas. The orebody is hosted in Lower Zechstein carbonates and shales and extends into Rotliegend sandstones. The roof is bedded calcareous dolomite overlain by massive anhydrite, while the floor is mainly quartz sandstone with clay cement underlain by red Rotliegend sandstone (Fig. 1), promoting separation along bedding and interfaces. The panel is weakly tectonised, with a small-throw normal fault (0.1–0.5 m) and preferential NE–SW and NW–SE roof cracking. It is classified as high rockburst risk, consistent with UCS values of ~120 MPa (roof), ~86 MPa (ore) and ~42 MPa (floor) and the seismicity context of deep copper mining.

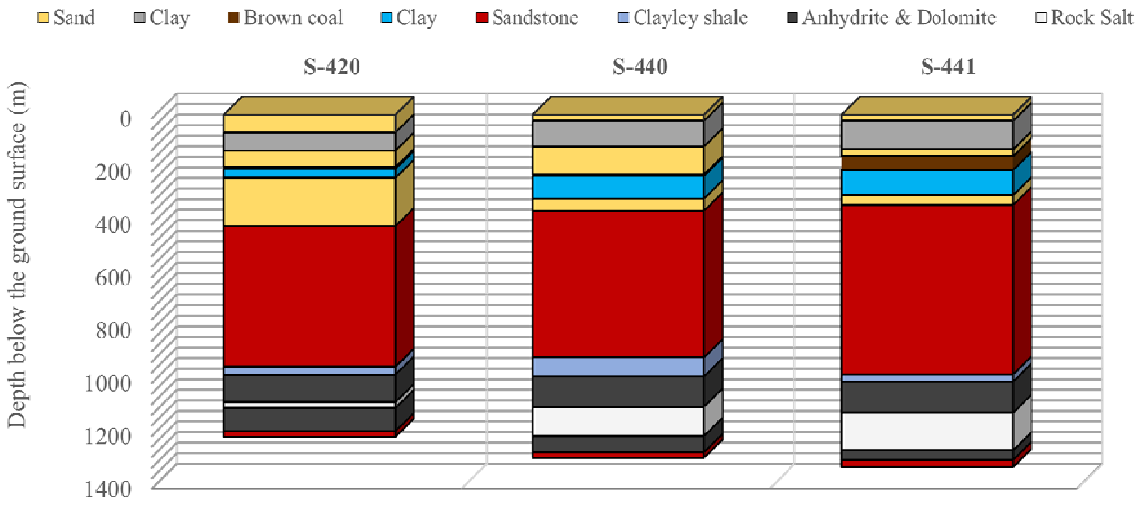


Fig. 1 Data from exploration boreholes in surrounding of analysed mining panel.

3 Material and Methods

The workflow used to compare room-and-pillar variants consisted of four steps: (1) development of a full-scale 3D FEM model representing the panel geometry and main lithological units, (2) iterative calibration using underground convergence measurements, (3) staged simulations of three pillar-size variants under consistent assumptions, and (4) variant ranking based on combined safety indicators and a recovery-based economic screening.

3.1 Numerical Model

A large-scale 3D finite element model was built in GTS NX. The geological framework was prepared from exploration drilling data around the analysed panel, and the model dimensions were 1.5 × 1.5 × 1.0 km to represent the large-scale loading conditions. To balance accuracy and computation time, a hybrid mesh (tetrahedral + hexahedral elements) with element-size gradation was used. The maximum element size at the deposit level was 1.5 m, while in layers far from the mining horizon it increased up to 35 m, since distant layers mainly provide loading and are not the focus of the analysis (Fig. 2).

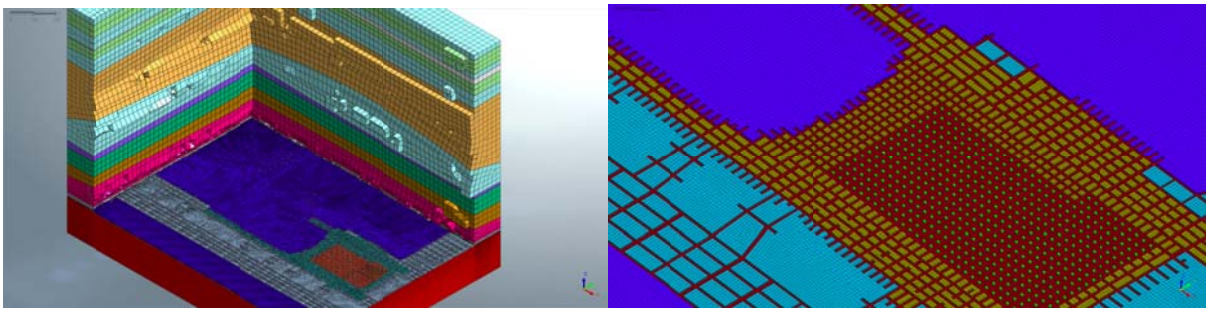


Fig. 2 Discretised 3D numerical model of analysed mining area (left) and view of the dense-mesh area which was base for model calibration (right).

Rock mass behaviour was represented with the Generalized Hoek–Brown (GHB) criterion. Initial parameters at the deposit level served as a baseline (Table 1) and were later reduced during calibration using GSI and disturbance (D) concepts to reflect in-situ degradation.

Table 1. Intact rock data at the excavation level.

Parameter	R_c [MPa]	E_s [GPa]	Cohesion, c [MPa]	Angle of friction, $\emptyset$ [°]	Poisson's ratio, ϑ [-]	Density, ρ [g/cm^3]	m_i [-]
Value	45.0	33.5	20.5	32	0.22	2.28	8

3.2 Calibration

Calibration was performed to ensure that the full-scale model reproduces realistic deformation trends and contrasts between excavation zones. The main dataset consisted of convergence measurements from telescopic convergence indicators installed between the roof and the floor. These measurements typically have low reading frequency (often once per day), so calibration focused on representative convergence levels and spatial patterns rather than short-term fluctuations. The location of convergometers and result of 1-month long convergence measurements are presented in Fig. 3.

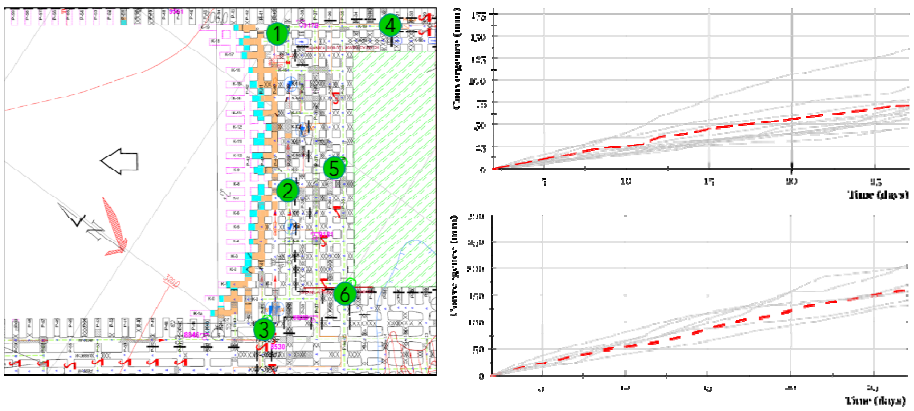


Fig. 3 Location of convergometers (left) and result of convergence measurement (right).

A key mismatch observed in early runs was an underestimation of the difference between the mining front zone and long-life excavations. To address this, rock mass strength reduction was applied separately in four geological-structural zones: technological pillars, backfilled/liquidated zones, intact rock mass, and large protective pillars. Each zone was assigned different GSI and D parameters within the GHB framework to capture varying degrees of mining-induced damage and discontinuity.

3.3 Pillar geometries

After calibration, three pillar geometries were evaluated: 4×4 m, 5×6 m, and 8×8 m. To capture the effect of mining advance, three stages of front progress were simulated for each variant (Fig. 4). In the liquidation phase, remnant pillars were kept identical across all scenarios (4×3 m), ensuring comparability and isolating the influence of technological pillar geometry.

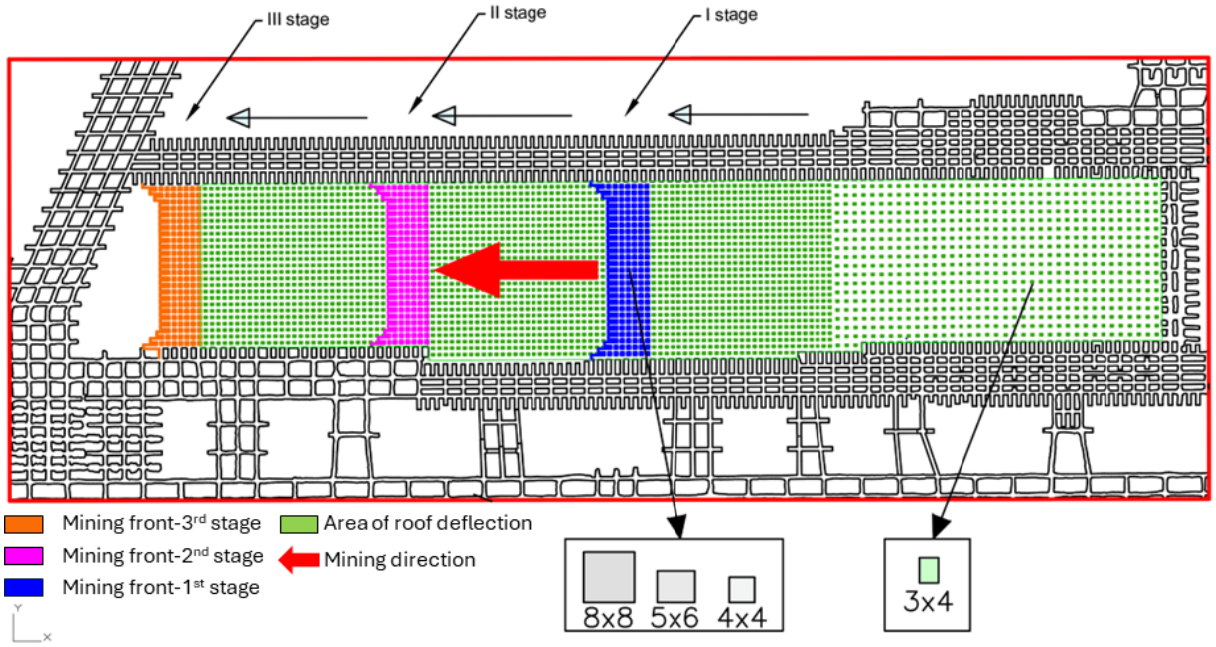


Fig. 4 Considered exploitation scenarios with marked stages of mining front line.

4 Results and discussion

The calibration was performed through iterative updates of the Hoek–Brown rock-mass parameters by adjusting GSI and the disturbance factor D separately in the main model zones, until a satisfactory match of displacement levels was obtained. The goal was achieved after the third iteration for both the active exploitation area and the long-life entries (haulage and ventilation drifts). The exact values of nonlinear GSI parameters are presented in Table 2.

For the purposes of this study, the analysis focused on the distribution of the stability indicator FS at the ore level along a cross-section, covering the transition from undisturbed rock mass, through the active mining front, to the mined-out area behind the front(Fig. 5).After model calibration, three room-and-pillar variants were simulated with staged mining progress (Stages I–III). To ensure direct comparability, the same liquidation approach was applied in all cases, i.e., identical 4×3 m remnant pillars in the liquidation zone.

Table 2. Results of the third iteration of calculations (baseline response before calibration).

Parameter	Intact rock mass	Large pillars	Technological pillars	Goaf's (Liquidation) zone
GSI	100	95	90	60
m_b	8.0000	6.6291	5.4376	1.1909
s	1.0000	0.5629	0.3105	0.0048
D	0.00	0.10	0.15	0.50
a	0.5	0.5001	0.5002	0.5028
E	33.50	31.05	24.15	9.10
c	9.7328	7.5400	5.8959	2.0641
φ	39.84	39.24	38.35	27.67

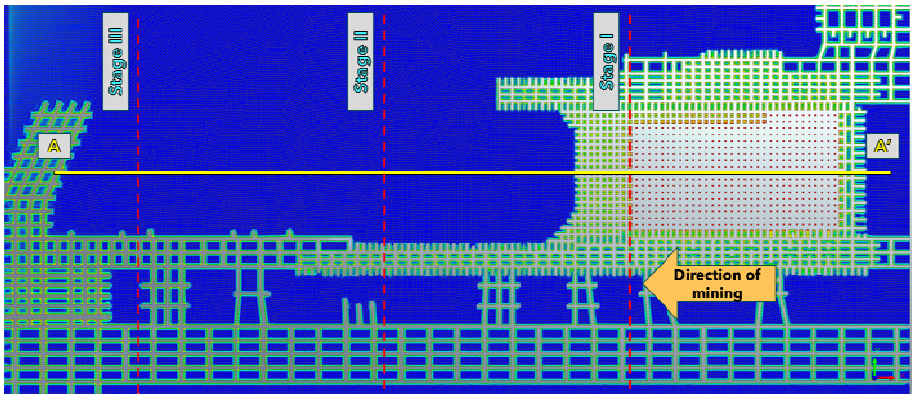


Fig. 5 3D numerical model view showing the location of the assessed cross-section (A-A´)and the three mining-advance stages (Stages I–III) defined by the position of the exploitation front used in the simulations.

All results are synthesised in Fig. 6 which presents the evolution of FS for each variant and stage.

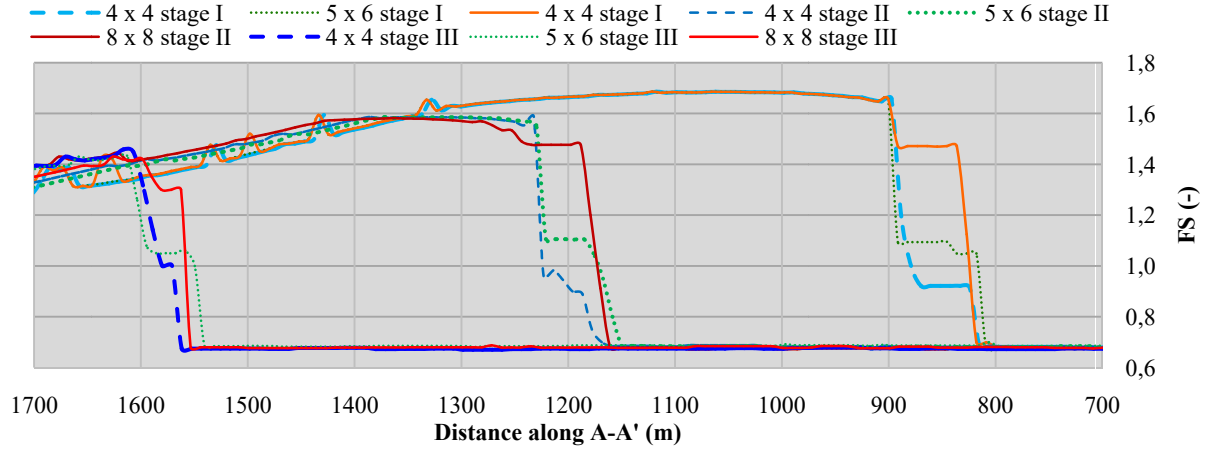


Fig. 6 Safety factor (FS) distribution at the deposit level along the A–A′ cross-section for three room-and-pillar variants (4×4 m, 5×6 m and 8×8 m pillars) in Stages I–III of mining advance.

The 4×4 m variant showed a relatively gentle, distributed roof response but consistently produced sections with FS < 1, indicating insufficient pillar capacity and clear instability risk; it was therefore rejected despite its “calmer” deformation character. By contrast, the 8×8 m variant maintained high FS values (FS≈1.45) at the mining front and between the front and liquidation, confirming strong stability margins during development, but it also introduced excessive stiffness early in the sequence. During liquidation (cutting to 4×3 m remnants), the model indicated a sudden, strongly localised loss of capacity and abrupt roof deflection—unfavourable at great depth because it may trigger dynamic cracking of stiff roof layers and contribute to high-energy seismic events and operational disruptions.
The 5×6 m variant provided the most balanced behaviour, with FS ≈ 1.1 and a more controlled, spatially distributed roof response than the 8×8 m case. Recovery was 93% (8×8 m), 90% (5×6 m) and 87% (4×4 m). Although 8×8 m maximises extraction, the higher likelihood of sudden deformation during liquidation may offset this benefit through downtime and added support costs. Therefore, the 5×6 m layout was identified as the best safety–economics compromise, combining high recovery with stable, predictable response.

5 Conclusions

The calibrated full-scale 3D FEM analyses show that variant selection in deep room-and-pillar mining is controlled not only by recovery but also by how stability and deformation evolve during mining advance and, most importantly, during the transition to liquidation. The 4×4 m variant was rejected due to persistent instability indicators (FS < 1). The 8×8 m variant provided the highest recovery, but the model indicated an unfavourable stiff-to-post-critical response with a sudden, localised loss of load-bearing capacity during pillar cutting, which may increase the likelihood of abrupt roof deflection and higher seismic/dynamic hazard. The 5×6 m layout delivered the best safety–economics compromise, combining acceptable stability margins (FS ~ 1.1) with high recovery (~90%) and a more controlled roof response across the analysed stages.

From a methodological perspective, the key advantage of the proposed workflow is that it converts large-scale 3D modelling into a decision-support tool by combining staged analysis with spatial calibration against field convergence data. Adjusting GSI and disturbance factor D independently in the main geomechanical zones allowed the model to reproduce deformation levels both in the active extraction area and in long-life entries, improving confidence in scenario ranking. This approach is implementable in routine mine planning: once a calibrated "panel-scale" model is established, alternative layouts and liquidation strategies can be screened consistently, safety-critical zones can be identified early, and numerical results can be directly linked to practical design rules (pillar geometry, sequencing, support needs) and recovery-based economic constraints.

References

Benz, T., Schwab, R., Kauther, R.A. and Vermeer, P.A. (2008) A Hoek–Brown criterion with intrinsic material strength factorization. International Journal of Rock Mechanics and Mining Sciences, 45(2): 210–222.

Esterhuizen, G.S., Dolinar, D.R. and Ellenberger, J.L. (2011) Pillar strength in underground stone mines in the United States. International Journal of Rock Mechanics and Mining Sciences, 48(1): 42–50.

Fuławka, K., Pytel, W. and Mertuszka, P. (2018) The effect of selected rockburst prevention measures on seismic activity – Case study from the Rudna copper mine. Journal of Sustainable Mining, 17(1): 1–10.

Fuławka, K., Kwietniak, A., Lay, V. and Jaśkiewicz-Proć, I. (2022) Importance of seismic wave frequency in FEM-based dynamic stress and displacement calculations of the earth slope. Studia Geotechnica et Mechanica, 44(1): 82–96.

Fuławka, K., Kołodziej, R., Stolecki, L. and Jaśkiewicz-Proć, I. (2024) The use of large-scale 3D numerical modelling to identify areas of increased seismic risk in Polish underground copper mines. Proceedings of the 7th International Conference on Geotechnical and Geophysical Site Characterization (ISC'7), Barcelona, Spain, 18–21 June 2024.

Hedley, D.G.F. and Grant, F. (1972) Stope-and-pillar design for the Elliot Lake uranium mines. CIM Bulletin, 65: 37–44.

Hoek, E., Marinos, P. and Benissi, M. (1998) Applicability of the Geological Strength Index (GSI) classification for very weak and sheared rock masses: The case of the Athens Schist Formation. Bulletin of Engineering Geology and the Environment, 57(2): 151–160..

Hoek, E., Carranza-Torres, C. and Corkum, B. (2002) Hoek–Brown failure criterion – 2002 Edition. In: Hammah, R., Bawden, W., Curran, J. and Telesnicki, M. (eds) Proceedings of NARMS–TAC 2002: Mining Innovation and Technology, Toronto, Canada, 10 July 2002, pp. 267–273. University of Toronto, Toronto.

Jing, L. (2003) A review of techniques, advances and outstanding issues in numerical modelling for rock mechanics and rock engineering. International Journal of Rock Mechanics and Mining Sciences, 40(3): 283–353.

Malli, T., Yetkin, M.E., Özfirat, M.K. and Kahraman, B. (2017) Numerical analysis of underground space and pillar design in metalliferous mine. Journal of African Earth Sciences, 134: 365–372.

Marinos, V., Marinos, P. and Hoek, E. (2005) The Geological Strength Index: Applications and limitations. Bulletin of Engineering Geology and the Environment, 64(1): 55–65.

Martin, C.D. and Maybee, W.G. (2000) The strength of hard-rock pillars. International Journal of Rock Mechanics and Mining Sciences, 37(8): 1239–1246.

Pytel, W., Fuławka, K., Pałac-Walko, B. and Mertuszka, P. (2023) Numerical and analytical determination of rockburst characteristics: Case study from Polish deep copper mine. Applied Sciences, 13(21): 11881.

Rafiei Renani, H. and Martin, C.D. (2018) Modeling the progressive failure of hard rock pillars. Tunnelling and Underground Space Technology, 74: 71–81.

Shapka-Fels, T. and Elmo, D. (2022) Numerical modelling challenges in rock engineering with special consideration of open pit to underground mine interaction. Geosciences, 12(5): 199.

Sinha, S. and Walton, G. (2019) Numerical analyses of pillar behavior with variation in yield criterion, dilatancy, rock heterogeneity and length to width ratio. Journal of Rock Mechanics and Geotechnical Engineering, 11(3): 521–536.

Theron, W.J. and Malan, D.F. (2024) Pillar design and the associated mining engineering constraints in hard rock bord-and-pillar mines. Journal of the Southern African Institute of Mining and Metallurgy, 124(11): 631–644.